Fundamenta Informaticae 125 (2013) 223–237
DOI 10.3233/FI-2013-861
IOS Press

Discrete Tomography in MRI: a Simulation Study

Hilde Segers[*†]
iMinds – Vision Lab, University of Antwerp, Belgium
hilde.segers@ua.ac.be

Willem Jan Palenstijn
iMinds – Vision Lab, University of Antwerp, Belgium
willemjan.palenstijn@ua.ac.be

Kees Joost Batenburg
Centrum voor Wiskunde en Informatica, Amsterdam, The Netherlands
K.J.Batenburg@cwi.nl

Jan Sijbers
iMinds – Vision Lab, University of Antwerp, Belgium
jan.sijbers@ua.ac.be

Abstract. Discrete tomography (DT) is concerned with the tomographic reconstruction of images that consist of only a small number of grey levels. Recently, DART, a practical algorithm was introduced for discrete tomography, which was validated in the domain of X-ray computed and electron tomography. In this paper, DART is introduced for magnetic resonance imaging. Using simulation experiments, it is shown that the proposed MRI-DART algorithm is capable of computing high quality reconstructions from substantially fewer data compared to state-of-the-art MRI reconstruction methods.

[*]This work was financially supported by the iMinds-SuperMRI project (Interdisciplinary Institute for Technology, a research institute founded by the Flemish Government) and by the TOP BOF project Quantitative Tomographic Segmentation of Magnetic Resonance Images.
[†]Address for correspondence: iMinds – Vision Lab, University of Antwerp, Universiteitsplein 1 (N.115), B-2610 Antwerpen, Belgium

1. Introduction

Magnetic Resonance imaging (MRI) is a well-known non-invasive experimental technique that uses a strong magnetic field and non-ionizing radiation to produce images of various structures like organs, soft tissues, bone, or biological samples. MRI allows for structural investigations of a variety of complex systems relevant to problems in health care, biology, industry, and materials science.

In MRI, the object is sampled in Fourier space (k-space). Conventionally, Cartesian k-space sampling is applied, which only requires a simple inverse fast Fourier transform (FFT) to reconstruct the image. More sophisticated image reconstruction methods have been proposed for non-Cartesian k-space acquisitions. In particular, compressed sensing (CS) methods are becoming increasingly popular in MRI [10, 15, 16]. CS aims to reconstruct signals and images from significantly fewer measurements than were traditionally thought necessary. Such methods exploit sparseness in some transform domain, which is an intrinsic kind of prior knowledge, to maintain image quality. It has been shown that if the image is sparse, it can be reconstructed accurately from a small number of measurements with very high probability, as long as the set of measurements satisfies certain randomization properties [9]. In many images of objects that are imaged in practice, the image itself is not sparse, yet the boundary of the object is relatively small compared to the total number of pixels. In such cases, sparsity of the gradient image can be exploited by, for example, Total Variation Minimization [8, 13].

In this paper, a new type of prior knowledge on the grey levels in the MRI image is exploited. Many objects are composed of regions that can be well represented by a single material/tissue. Clear examples are water-silicone breast implants [12, 14, 17]. Also, in an angiogram, the image can be well represented by either background or vascular structure [11]. Alternatively, a human brain can be roughly classified into white, grey matter, and cerebro spinal fluid (CSF) [22]. In food processing, MRI of apples (e.g., for detection of internal browning) reveals clear tissue classes [3].

Prior knowledge on the image grey levels is exploited in discrete tomography (DT), a technique that is concerned with the problem of recovering images from their projections where the images are assumed to consist of a small number of grey values only. DT has already been successfully applied to a broad range of material samples in electron tomography [2, 4, 20], X-ray attenuation tomography [5, 21], and X-ray diffraction tomography [7]. It has been shown that, similar to CS, DT may lead to significantly improved image reconstructions from only a fraction of the traditionally acquired data.

In this paper, we will introduce the concept of discrete tomography in the domain of magnetic resonance imaging and compare its effectiveness to standard iterative reconstruction schemes.

After introduction of the MR imaging model and the basic concepts and notation, the methodology behind discrete tomography for MRI is explained. Finally, in Section 4, simulation results are presented and discussed.

2. Methods

2.1. MR imaging model

Magnetic resonance imaging is based on the nuclear spin of hydrogen atoms of the object to be imaged. In a strong external magnetic field $\vec{B}_0$, these spins will align with the external field, yielding a net magnetic moment oriented parallel to $\vec{B}_0$. By sending radio frequency signals to the object at resonance frequency (the so-called Larmor frequency), energy is absorbed, which causes the magnetization to tilt

with respect to its original direction. This produces a magnetization component m transverse to the external field, precessing at the Larmor frequency and generating an electromagnetic signal that can be picked up by receiver coils. The received signal from all precessing magnetizations $m(\vec{r})$ in the object yields information about physical properties of tissue, such as the proton density and relaxation parameters.

Spatial information is encoded in the MR signal by superimposing additional, spatially varying magnetic fields $G(x, y, z)$ on top of B_0. These magnetic field gradients establish a Fourier relation between the received radio frequency MR signal and the magnetization distribution. Multidimensional spatial encoding can be understood by introducing the notion of k-space. In the so-called phase encoding direction, a linear phase dispersion develops due to the gradient-induced linear variation in precession frequency. Therefore, the receiver coil detects a signal encoded by the linear phase. It can be shown that the signal equation in MRI has the form of a Fourier integral, with an extra rate map factor to model inhomogeneities in the magnetic fields and decay of the signal due to natural dephasing,

$$s(t) = \int_V m(\vec{r}) \mathrm{e}^{-i2\pi\vec{k}(t)\cdot\vec{r}} \mathrm{e}^{-z(\vec{r})t} d\vec{r}, \tag{1}$$

where $k(t) = \int_0^t G(\vec{\tau}) d\vec{\tau}$ and $z(\vec{r})$ is the rate map. In this paper we restrict ourselves to the case where the rate map is zero, so that the received signal s at time t is the Fourier transform of the transverse magnetization $m(\vec{r})$ sampled at a spatial frequency $k(t)$. In practice, the received signal is sampled at discrete times t_i, yielding an ill-posed continuous-discrete problem because there are a multitude of continuous-space solutions m that exactly match the measured data $\boldsymbol{s} = (s(t_1), s(t_2), \ldots, s(t_M))$. By discretizing m on a rectangular grid, the reconstruction problem simplifies to determining the vector of unknown grey values $\boldsymbol{m} = (m_1, \ldots, m_N)$ from the measurement vector $\boldsymbol{s}$, by solving the linear model,

$$\boldsymbol{s} = \boldsymbol{A}\boldsymbol{m} + \boldsymbol{\epsilon}, \tag{2}$$

where $\boldsymbol{\epsilon}$ represents Gaussian noise. The $M \times N$ *encoding matrix* $\boldsymbol{A}$ has elements

$$a_{ij} = e^{-i2\pi\vec{k}(t_i)\cdot\vec{r}_j} \tag{3}$$

where $i = 1, \ldots, M$ and $j = 1, \ldots, N$.

2.2. Discrete tomography

In this paper, we consider the reconstruction of MR magnitude images that consist of only a few different grey values, which are assumed to be known a priori. Formally, the problem can be expressed as follows:

Problem: Let $\boldsymbol{A}^{M\times N}$ be a given Fourier encoding matrix and $\boldsymbol{s} \in \mathbb{C}^M$ be a vector of measured k-space data. Let $l > 0$ be the prescribed number of grey values and $R = \{\rho_1, \ldots, \rho_l\}$ denote the set of grey values. Find $\boldsymbol{m} \in \mathbb{C}^N$ such that $|\boldsymbol{m}| \in R^N$ and $\boldsymbol{A}\boldsymbol{m} = \boldsymbol{s}$.

Since the set R^N is not convex, many algorithms for convex optimization that can be used to solve the general algebraic reconstruction problem cannot be used directly for discrete tomography.

2.3. The MRI-DART algorithm

Batenburg and Sijbers [6] introduced the Discrete Algebraic Reconstruction Technique (DART) for solving discrete tomography reconstruction problems. The algorithm has been successfully applied in the domains of Computed Tomography (CT) and Electron Tomography (ET) [1] [4], but has not yet been introduced in MRI reconstruction problems. We will now describe DART adapted to MRI, which will be referred to as MRI-DART.

MRI-DART alternates between "continuous" update steps where the reconstruction is considered as an array of complex-valued unknowns, and discretization steps, which incorporate prior knowledge about the grey values in the image. Various algebraic reconstruction methods (ARM) can be employed for the continuous step (e.g., SIRT, CGLS, LSQR). The experiments in this paper were carried out with the LSQR method [19] as a subroutine. This is an iterative method, which efficiently approximates least squares solutions for large systems of linear equations.

Fig. 1 depicts a flowchart of MRI-DART.

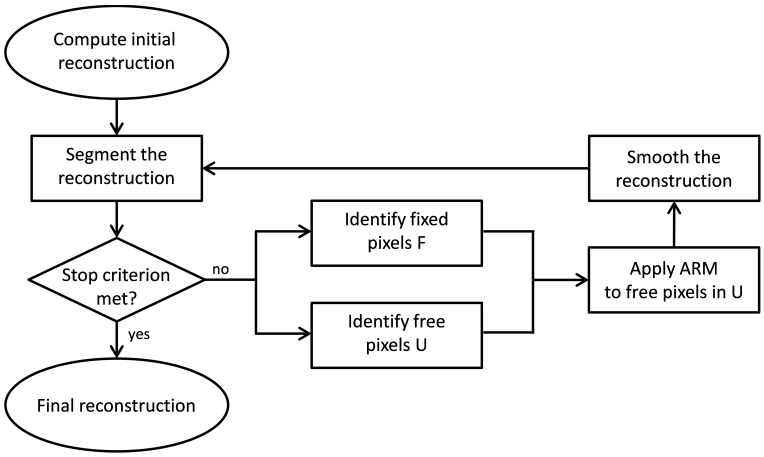

Figure 1: Flowchart of MRI-DART

As a starting point, a first continuous reconstruction $m^{(0)}$ is computed using LSQR. Subsequently, a number of MRI-DART iterations is performed, which consist of following steps:

1. **Segmentation:** The current continuous image is segmented to obtain a segmentation $\boldsymbol{g}^{(t)}$ where the grey values are in the set of real numbers $R = \{\rho_1, \ldots, \rho_l\}$. In this work, a simple thresholding scheme is employed on the magnitude image, with thresholds

$$\tau_i = \frac{\rho_i + \rho_{i+1}}{2}. \tag{4}$$

The threshold function $r : \mathbb{C} \to R$ is defined as

$$r(x) = \begin{cases} \rho_1 & (|x| < \tau_1) \\ \rho_2 & (\tau_1 \leq |x| < \tau_2) \\ \quad \vdots & \\ \rho_l & (\tau_{l-1} \leq |x|) \end{cases} \tag{5}$$

Since the experiments in this paper are carried out on simulation data, generated from real (as opposed to complex) image data, all phase information is discarded by the threshold function $r(x)$.

2. **Termination criterion:** As MRI-DART is a *heuristic algorithm*, there is no formal statement of convergence. In this work, we run the algorithm for a fixed number of 15 iterations. As an alternative, the *total projection error* $E : R^N \to \mathbb{R}$, defined as

$$E(\boldsymbol{g}) = \|\boldsymbol{A}\boldsymbol{g} - \boldsymbol{s}\|_2 \tag{6}$$

can be used.

3. **Identify 'fixed' and 'free' pixels:** In this step, all pixels are classified into one of two categories: 'fixed' or 'free'. The 'fixed' pixels are assumed to have the correct grey value and will not be updated in this iteration. The following pixels are chosen as 'free' pixels:

   - **boundary pixels:** The set $B^{(t)} \subset \{1, \ldots, N\}$ of *boundary pixels* is computed from the segmentation $\boldsymbol{g}^{(t)}$, resulting from the first step. We denote the neighbourhood of pixel i by $P(i) \subset \{1, \ldots, N\}$. As a connectivity measure, the 8-connected neighbourhood is employed in the experiments in this paper. A pixel $g_i^{(t)}$ is called a boundary pixel if there exists a $j \in P(i)$ for which $g_j^{(t)} \neq g_i^{(t)}$. The set of free pixels $U^{(t)} \subset \{1, \ldots, N\}$ that will be updated in the next step is initialized by $U^{(t)} = B^{(t)}$.
   - **randomly other pixels:** Afterwards $U^{(t)}$ is augmented with non-boundary pixels in a randomized procedure. Let $0 < p \leq 1$ be the *fix probability*. Each element of the non-boundary pixels is added to $U^{(t)}$ with a probability of $1 - p$ independently. Each MRI-DART iteration, different pixels are randomly added to the free pixels, which allows for changes in image areas not adjacent to any of the boundary pixels. The experiments in this paper were carried out with a fix probability of $p = 0.85$.

   The remaining pixels are included in the set of fixed pixels $F^{(t)} = \{1, \ldots, N\} \setminus U^{(t)}$.

4. **Apply ARM on free pixels:** Consider the system of linear equations to be solved in MRI-DART iteration (t),

$$\begin{pmatrix} | & & | \\ \boldsymbol{a}_1 & \ldots & \boldsymbol{a}_N \\ | & & | \end{pmatrix} \begin{pmatrix} m_1^{(t)} \\ \vdots \\ m_N^{(t)} \end{pmatrix} = \boldsymbol{s}, \tag{7}$$

   where $\boldsymbol{a}_i$ denotes the ith column of the Fourier encoding matrix $\boldsymbol{A}$. For all pixels $i \in F^{(t)}$, the grey value $m_i^{(t)}$ is fixed at the segmented value $g_i^{(t)}$. This transforms the system in equation (7) into

the new system

$$\begin{pmatrix} | & & | & | & & | \\ \boldsymbol{a}_1 & \dots & \boldsymbol{a}_{j-1} & \boldsymbol{a}_{j+1} & \dots & \boldsymbol{a}_N \\ | & & | & | & & | \end{pmatrix} \begin{pmatrix} m_1^{(t)} \\ \vdots \\ m_{j-1}^{(t)} \\ \\ m_{j+1}^{(t)} \\ \vdots \\ m_N^{(t)} \end{pmatrix} = \boldsymbol{s} - g_j^{(t)} \boldsymbol{a}_j. \tag{8}$$

While the number of equations in the new system $\tilde{\boldsymbol{A}}\tilde{\boldsymbol{m}} = \tilde{\boldsymbol{s}}$ remains the same, the number of unknown variables is vastly reduced to $N - |F^{(t)}|$. As mentioned previously, LSQR is employed as ARM to solve the system in a fixed amount of iterations. If the grey values of the fixed pixels were correct (matching the unknown true underlying object), solving this reduced system will result in better values for the remaining free pixels.

5. **Smoothing:** A smoothing operation is applied to the resulting image $\boldsymbol{m}^{(t)}$, in order to remove heavy fluctuations in the values of the free pixels. These fluctuations originate from noise-fitting (since the noise power in the k-space data $\boldsymbol{s}$ is now distributed among fewer pixels), as well as from grey value errors in the fixed (and thus assumed to be correct) pixels. In this work, a Gaussian filter with a radius of 1 pixel is applied to smooth the reconstruction.

2.4. Implementation

We have implemented the MRI-DART algorithm in Matlab. Instead of keeping the Fourier encoding matrix $\boldsymbol{A}$ explicitly in memory, all entries are computed on the fly as they are needed in the algorithm. The multiplications with $\boldsymbol{A}$ and $\boldsymbol{A}^{\mathrm{T}}$ are the computationally most challenging operations in the LSQR algorithm. They are implemented on the *graphical processing unit* (GPU) to improve algorithm performance due the specific hardware architecture which is well equipped for parallel operations.

3. Experiments

In this section, we describe the simulation experiments that were carried out to evaluate the reconstruction performance of MRI-DART and to compare it with a commonly used reconstruction method.

3.1. Phantoms

The simulation experiments were based on 4 phantom images, shown in Fig. 2.

(a) Phantom 1: represents a very simple, binary object. The size of this phantom is 256×256 pixels.

(b) Phantom 2: represents a binary resolution object with a high complexity, whose size equals 256×256 pixels. It contains holes of varying sizes, which is, as will become apparent from the results, more difficult to reconstruct accurately than phantom 1.

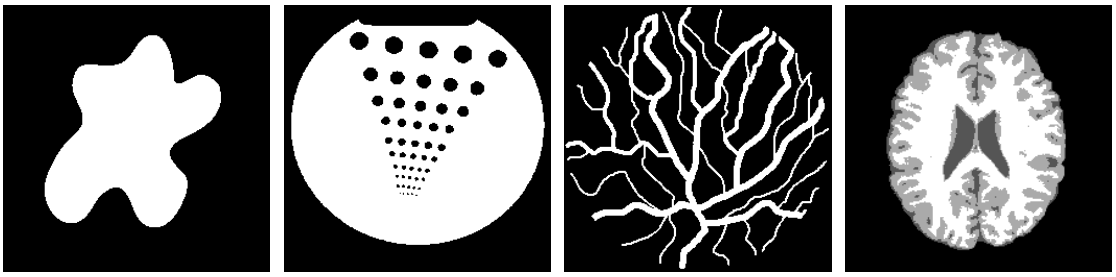

(a) Phantom 1 (b) Phantom 2 (c) Phantom 3 (d) Phantom 4

Figure 2: Phantom images used for the simulation experiments

(c) Phantom 3: is a binary image which mimics an angiography scan of 256×256 pixels and represents blood vessels.

(d) Phantom 4: represents a human brain, consisting of 4 different grey values (representing white matter, grey matter, CSF and background). Its size is 219×219 pixels.

Two different k-space trajectories $\vec{k}(t)$ were employed to simulate the k-space data, which lead to very different undersampling patterns. These trajectories are displayed in Fig. 3. The thin lines represent a full k-space, where the thick lines indicate the undersampling strategy.

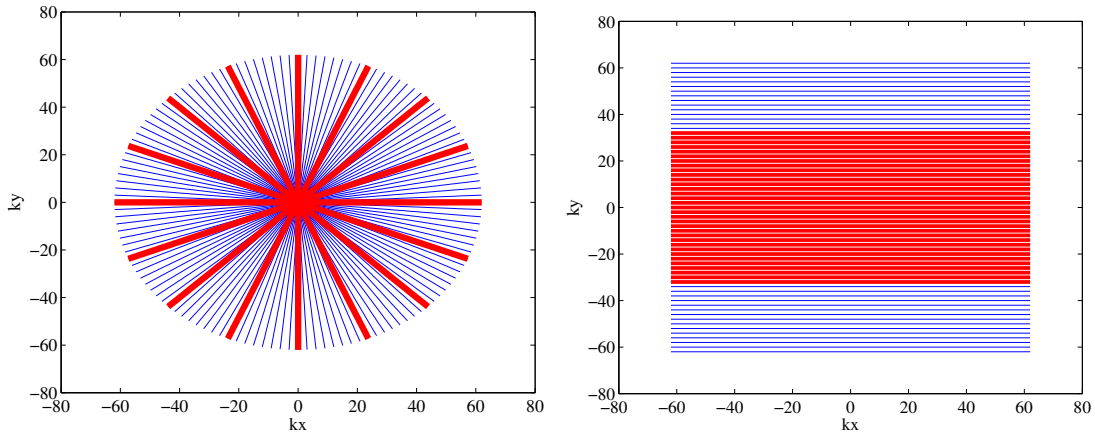

(a) Radial trajectory (b) Cartesian trajectory

Figure 3: The k-space trajectories and undersampling strategies that were employed in the simulation experiments.

(a) Radial trajectory: 9 different patterns with equiangular spokes were simulated, where the number of spokes ranged from 20 to 60. The number of samples per spoke was equal to the width w in pixels of the phantom image.

(b) Cartesian trajectory: 9 different patterns were simulated with a number of phase encoding lines (direction k_y) centered around the origin of k-space ranging from 20 to 60. The frequency encoding

direction (along k_x) was fully sampled (i.e., with a number of samples equal to the width w in pixels of the phantom image).

3.2. Quantitative comparison

An important feature of MRI-DART (and all discrete tomography algorithms) is the combination of reconstruction and segmentation into one single algorithm. We compared its performance to a more conventional approach where the k-space data was first reconstructed to a 'continuous' image, after which a separate post-processing segmentation algorithm was employed. The IMPATIENT-toolbox [23] was used to perform the reconstruction of the k-space data, which integrates the CGLS algorithm (40 iterations), inside a *total variation minimization* (TVM) regularization (10 iterations). These reconstructed images were then segmented using the well known Otsu segmentation [18], yielding the required discrete set of grey values.

4. Results and Discussions

In this section, we first present and compare the results obtained with MRI-DART and IMPATIENT+Otsu. Next, the performance of the radial and Cartesian undersampling strategies are compared. We consider the reconstruction accuracy of MRI-DART as a function of the number of phase encoding lines/spokes. The *relative number of misclassified pixels* (rNMP) is employed as the accuracy measure, and gives the ratio of the number of misclassified pixels to the total number of pixels.

4.1. Cartesian k-space sampling

Fig. 4 compares reconstruction performance of MRI-DART and IMPATIENT+Otsu in terms of rNMP as a function of the number of k-space lines for all 4 phantoms. The results show that MRI-DART consistently yields more accurate reconstructions. For phantom 1, Otsu's method yields a seemingly unexpected pattern where a larger number of phase encoding lines does not necessarily correspond to a smaller rNMP. According to Otsu's method, the optimal threshold for segmentation is the threshold for which the inter-class variance is maximized. For any number of phase encoding lines, this inter-class variance is nearly constant for a wide range of thresholds in phantom 1. This results in large variations in optimal threshold between different numbers of phase encoding lines and significant differences in the corresponding rNMP's. Fig. 5 depicts the reconstructed images for both MRI-DART and IMPATIENT+Otsu for 20 and 60 phase encoding lines.

4.2. Radial k-space sampling

In the previous series of experiments, all data was sampled on a Cartesian grid. In this section, we present the results from radially sampled data with a similar degree of undersampling as the Cartesian data. Fig. 6 depicts the relative number of misclassified pixels (rNMP) as a function of the number of spokes, comparing MRI-DART and IMPATIENT+Otsu for all 4 phantoms. The results show that MRI-DART consistently yields more accurate reconstructions. Reconstructed images for 20 and 60 spokes are displayed in Fig. 7.

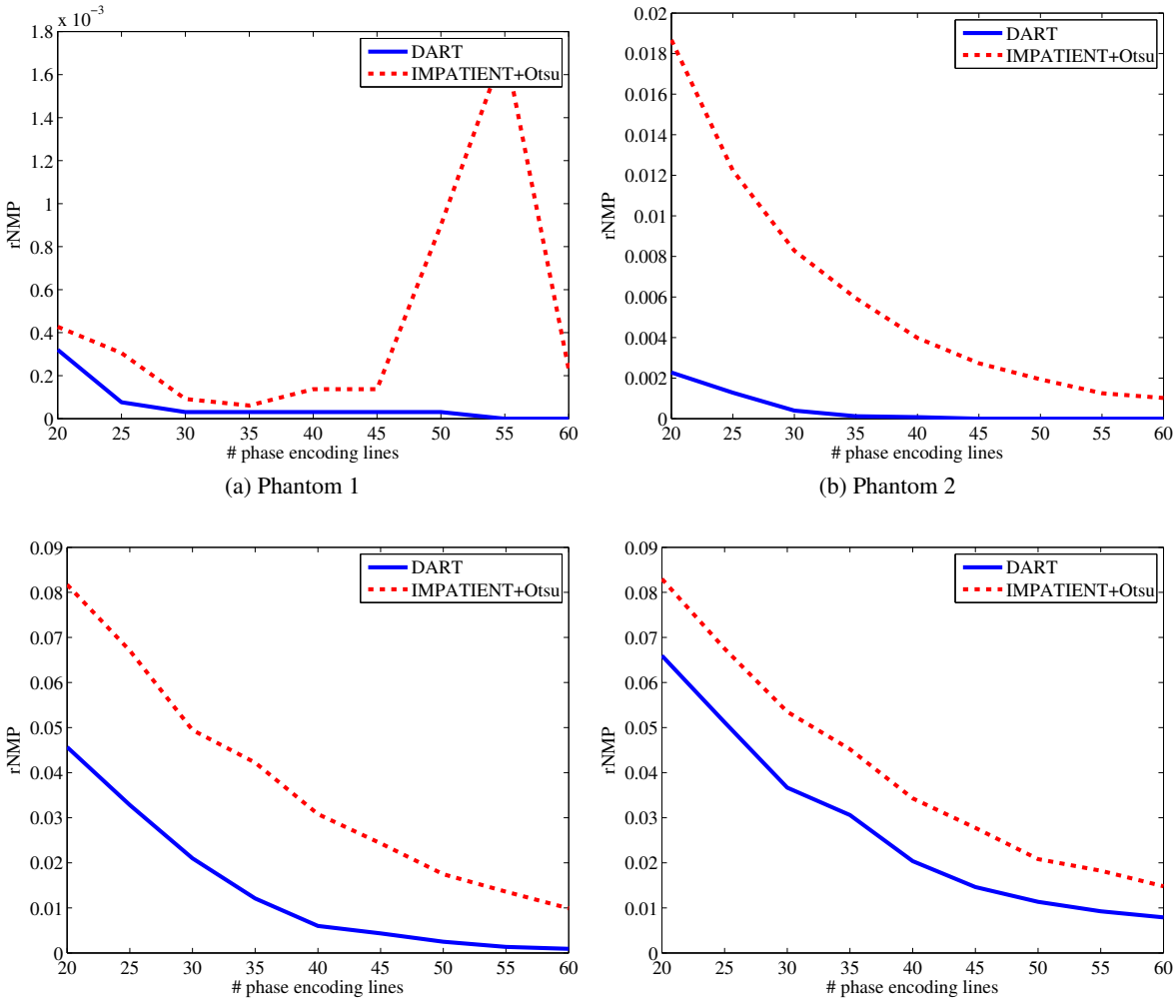

(a) Phantom 1

(b) Phantom 2

(c) Phantom 3

(d) Phantom 4

Figure 4: Comparison of rNMP between MRI-DART and IMPATIENT+Otsu for a different number of phase encoding lines

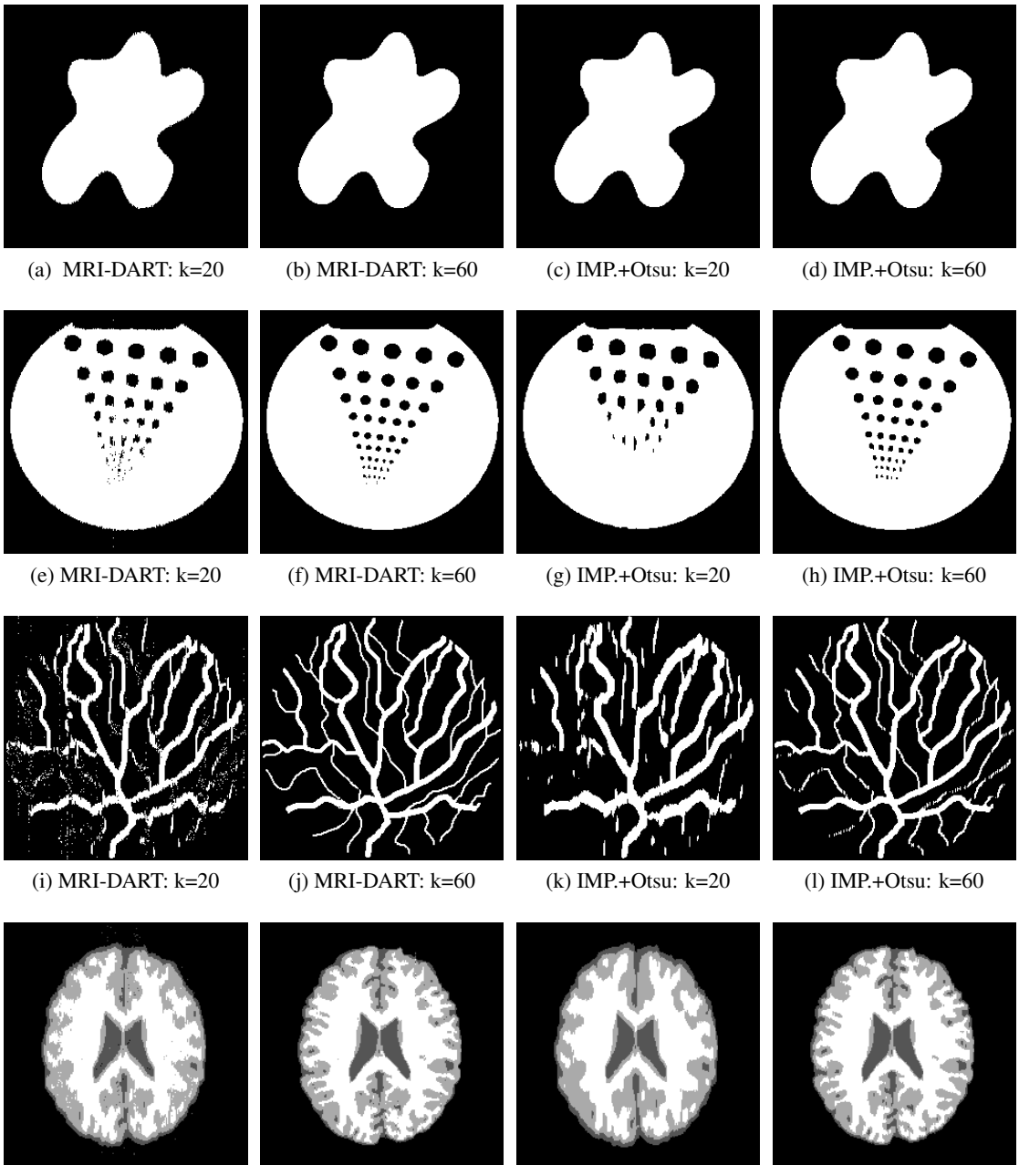

(a) MRI-DART: k=20 (b) MRI-DART: k=60 (c) IMP.+Otsu: k=20 (d) IMP.+Otsu: k=60

(e) MRI-DART: k=20 (f) MRI-DART: k=60 (g) IMP.+Otsu: k=20 (h) IMP.+Otsu: k=60

(i) MRI-DART: k=20 (j) MRI-DART: k=60 (k) IMP.+Otsu: k=20 (l) IMP.+Otsu: k=60

(m) MRI-DART: k=20 (n) MRI-DART: k=60 (o) IMP.+Otsu: k=20 (p) IMP.+Otsu: k=60

Figure 5: Reconstruction results for Cartesian sampling: comparing MRI-DART and IMPATIENT+Otsu for 20 and 60 phase encoding lines

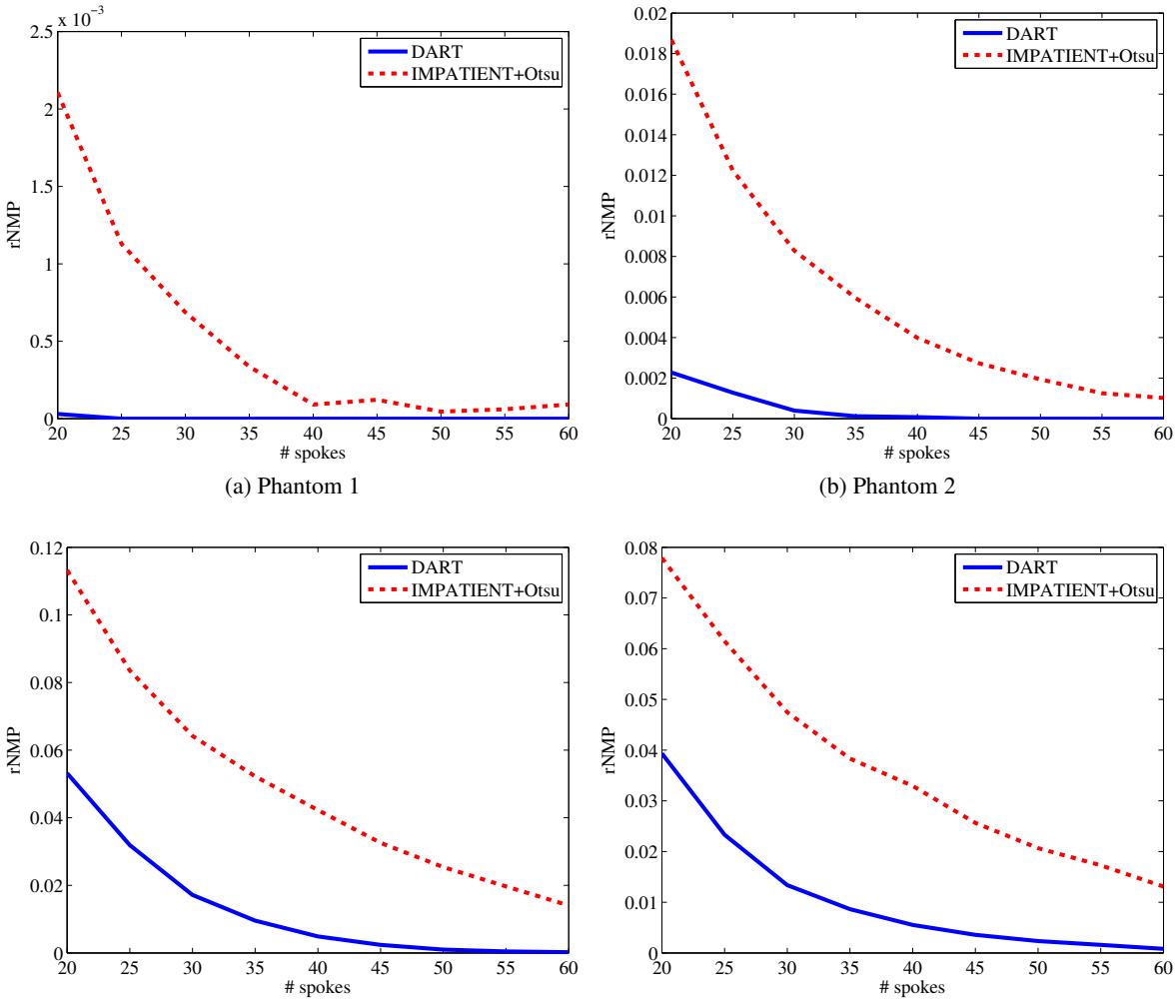

(a) Phantom 1

(b) Phantom 2

(c) Phantom 3

(d) Phantom 4

Figure 6: Comparison of rNMP between MRI-DART and IMPATIENT+Otsu for a different number of spokes

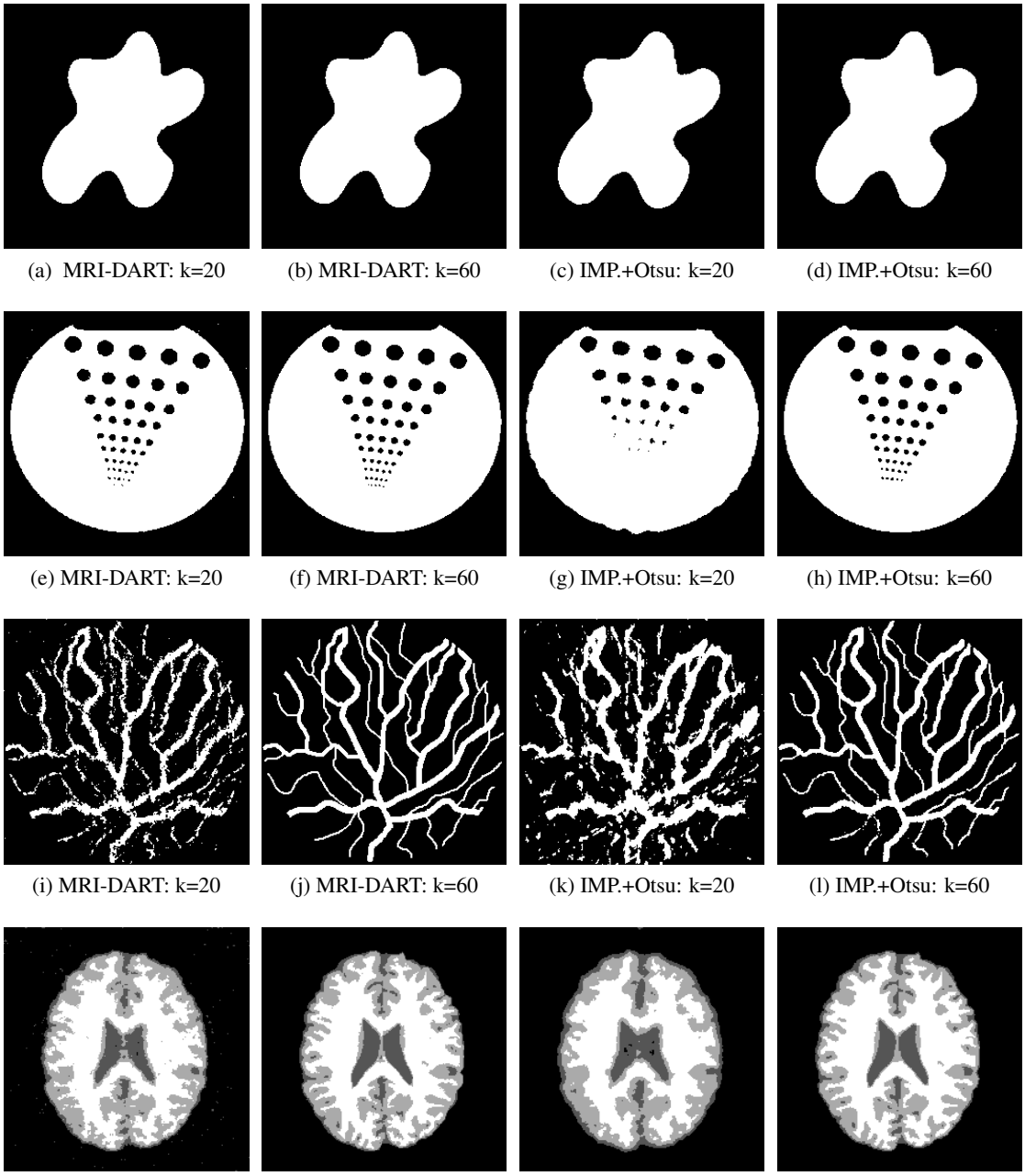

(a) MRI-DART: k=20 (b) MRI-DART: k=60 (c) IMP.+Otsu: k=20 (d) IMP.+Otsu: k=60

(e) MRI-DART: k=20 (f) MRI-DART: k=60 (g) IMP.+Otsu: k=20 (h) IMP.+Otsu: k=60

(i) MRI-DART: k=20 (j) MRI-DART: k=60 (k) IMP.+Otsu: k=20 (l) IMP.+Otsu: k=60

(m) MRI-DART: k=20 (n) MRI-DART: k=60 (o) IMP.+Otsu: k=20 (p) IMP.+Otsu: k=60

Figure 7: Reconstruction results for radial sampling: comparing MRI-DART and IMPATIENT+Otsu for 20 and 60 spokes

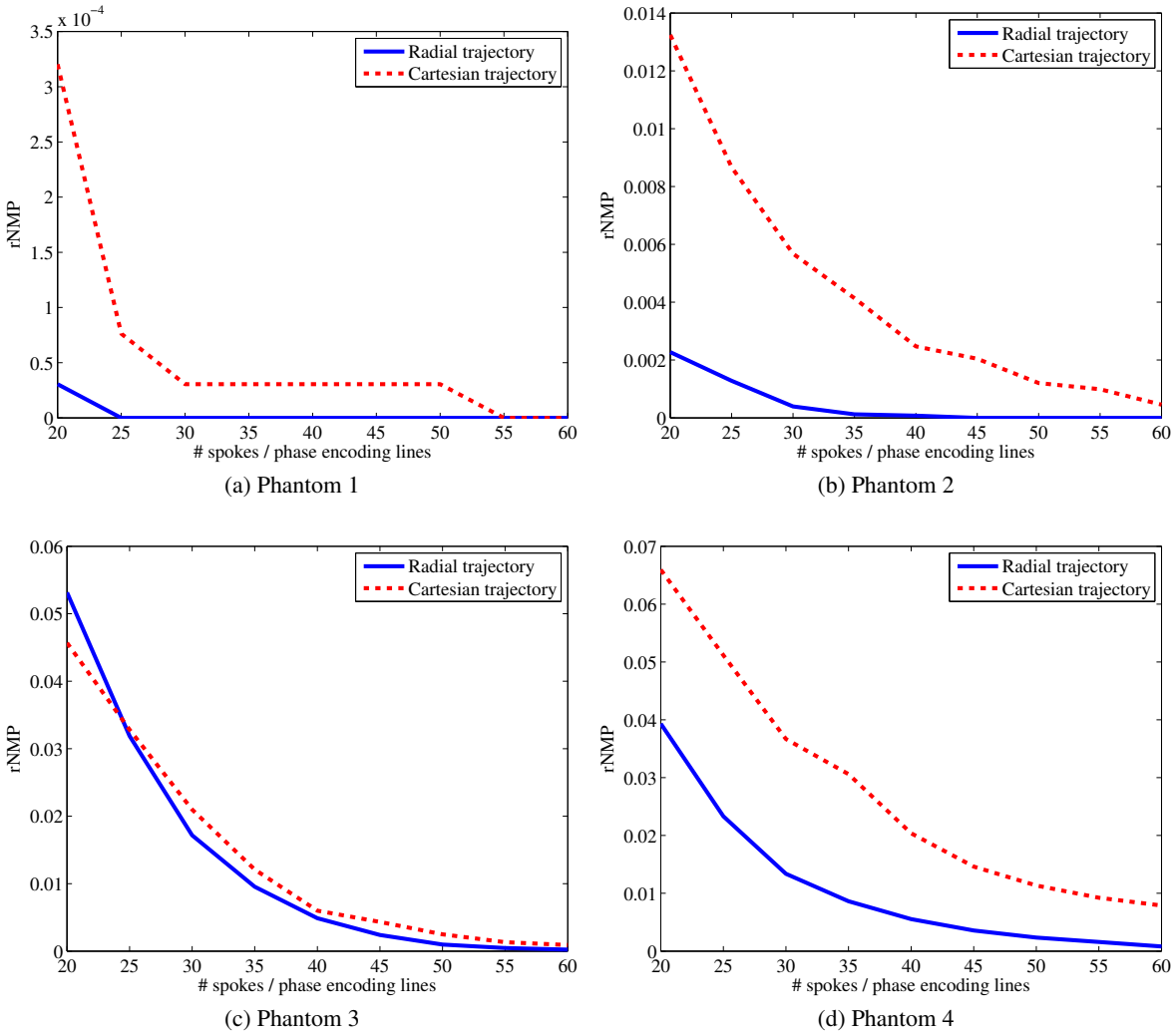

(a) Phantom 1

(b) Phantom 2

(c) Phantom 3

(d) Phantom 4

Figure 8: Comparison of rNMP between radial sampling MRI-DART and Cartesian sampling MRI-DART

4.3. Comparison Cartesian and radial k-space sampling

For comparison purposes, the number of data samples on a phase encoding line for Cartesian simulation sampling was set equal to the number of samples per spoke for radial sampling. Fig. 8 depicts the reconstruction accuracy in terms of rNMP for both trajectories as a function of the degree of undersampling. The reconstruction accuracy for phantom 3 is similar for both trajectories, while for the other phantoms the radial trajectory clearly gives more accurate results. The results for the Cartesian sampling of phantom 3 are due to the specific orientation of the vessels. When the simulations are repeated for a 90 degree rotated version of the vessels, the radial trajectory clearly outperforms the Cartesian trajectory again for the same degree of undersampling.

5. Conclusion

We have introduced the concepts of discrete tomography to the MR imaging model. The MRI-DART algorithm was employed to perform the discrete reconstruction from k-space data to image data. As a k-space trajectory, both Cartesian and radial (under)sampling were tested and compared. The results show that MRI-DART consistently yields more accurate reconstructions than the alternative IMPATIENT+Otsu segmentation technique. In general, the radial trajectory seems to yield more accurate results than the Cartesian trajectory, though the impact depends on the specific phantom. These preliminary simulation results seem to advice in favor of radial acquisition schemes in combination with MRI-DART, though further investigation is necessary to validate MRI-DART for real MRI applications. Future work will concentrate on investigating robustness against noise, automatic grey value estimation and expansion of the model to incorporate non-Fourier physical effects which corrupt real MRI data.

References

[1] Bals, S., Batenburg, K. J., Liang, D., Lebedev, O., Van Tendeloo, G., Aerts, A., Martens, J. A., Kirschhock, C. E. A.: Quantitative three-dimensional modeling of zeotile through discrete electron tomography, *Journal of the American Chemical Society*, **131**(13), 2009, 4769–4773.

[2] Bals, S., Batenburg, K. J., Verbeeck, J., Sijbers, J., Van Tendeloo, G.: Quantitative three-dimensional reconstruction of catalyst particles for bamboo-like carbon nanotubes, *Nano Letters*, **7**(12), 2007, 3669–3674.

[3] Barreiro, P., Ortiz, C., Ruiz-Altisent, M., Ruiz-Cabello, J., Fernández-Valle, M. E., Recasens, I., Asensio, M.: Mealiness assessment in apples and peaches using MRI techniques, *Magnetic Resonance Imaging*, **18**(9), 2000, 1175–1181.

[4] Batenburg, K. J., Bals, S., Sijbers, J., Kübel, C., Midgley, P. A., Hernandez, J. C., Kaiser, U., Encina, E. R., Coronado, E. A., Van Tendeloo, G.: 3D imaging of nanomaterials by discrete tomography, *Ultramicroscopy*, **109**(6), 2009, 730–740.

[5] Batenburg, K. J., Sijbers, J.: Discrete tomography from micro-CT data: application to the mouse trabecular bone structure, *Proceedings of SPIE Medical Imaging: Physics of Medical Imaging*, **6142**, February 2006, 1325–1335.

[6] Batenburg, K. J., Sijbers, J.: DART: A practical reconstruction algorithm for discrete tomography, *IEEE Transactions on Image Processing*, **20**(9), sept. 2011, 2542–2553.

[7] Batenburg, K. J., Sijbers, J., Poulsen, H. F., Knudsen, E.: DART: a robust algorithm for fast reconstruction of 3D grain maps, *Journal of Applied Crystallography*, **43**, 2010, 1464–1473.

[8] Block, K. T., Uecker, M., Frahm, J.: Undersampled radial MRI with multiple coils. Iterative image reconstruction using a total variation constraint, *Magnetic Resonance in Medicine*, **57**(6), 2007, 1086–1098.

[9] Candes, E. J., Wakin, M. B.: An introduction to compressive sampling, *IEEE Signal Processing Magazine*, **25**(2), march 2008, 21–30.

[10] Chartrand, R.: Fast algorithms for nonconvex compressive sensing: MRI reconstruction from very few data, *Proceedings of ISBI International Society of Biomedical Imaging*, July 2009, 262–265.

[11] El-Baz, A., Elnakib, A., Khalifa, F., El-Ghar, M. A., McClure, P., Soliman, A., Gimelfarb, G.: Precise segmentation of 3-D magnetic resonance angiography, *IEEE Transactions on Biomedical Engineering*, **59**(7), July 2012, 2019–2029.

[12] Elson, E. M., Jones, A., King, R., Chapman, P., Stanek, J., Irvine, A. T., Bingham, J. B.: Magnetic resonance imaging of trilucent TM breast implants, *Clinical Radiology*, **57**(4), 2002, 263–267.

[13] Feng, Y., Liu, P., Li, B., Yu, L., Chen, W.: Improved reconstruction of non-cartesian magnetic resonance imaging data through total variation minimization and POCS optimization, *Annual International Conference of the IEEE Engineering in Medicine and Biology Society (EMBC)*, sept. 2009, 2676–2679.

[14] Hölmich, L. R., Vejborg, I., Conrad, C., Sletting, S., McLaughlin, J. K.: The diagnosis of breast implant rupture: MRI findings compared with findings at explantation, *European Journal of Radiology*, **53**(2), 2005, 213–225.

[15] Lustig, M., Donoho, D., Pauly, J. M.: Sparse MRI: The application of compressed sensing for rapid MR imaging, *Magnetic Resonance in Medicine*, **58**(6), 2007, 1182–1195.

[16] Lustig, M., Donoho, D. L., Santos, J. M., Pauly, J. M.: Compressed Sensing MRI, *IEEE Signal Processing Magazine*, **25**(2), march 2008, 72–82.

[17] Madhuranthakam, A. J., Smith, M. P., Yu, H., Shimakawa, A., Reeder, S. B., Rofsky, N. M., McKenzie, C. A., Brittain, J. H.: Water-silicone separated volumetric MR acquisition for rapid assessment of breast implants, *Journal of Magnetic Resonance Imaging*, **35**(5), May 2012, 1216–1221.

[18] Otsu, N.: A Threshold Selection Method from Gray-Level Histograms, *IEEE Transactions on Systems, Man and Cybernetics*, **9**(1), 1979, 62–66.

[19] Paige, C. C., Saunders, M. A.: LSQR: An algorithm for sparse linear equations and sparse least squares, *ACM Transactions on Mathematical Software (TOMS)*, **8**(1), 1982, 43–71.

[20] Roelandts, T., Batenburg, K. J., Biermans, E., Kübel, C., Bals, S., Sijbers, J.: Accurate segmentation of dense nanoparticles by partially discrete electron tomography, *Ultramicroscopy*, **114**, 2012, 96–105.

[21] Van Gompel, G., Batenburg, K. J., Van de Casteele, E., Van Aarle, W., Sijbers, J.: A discrete tomography approach for superresolution micro-CT images, *Proceedings of ISBI International Society of Biomedical Imaging*, April 2010, 816–819.

[22] Weisenfeld, N. I., Mewes, A. J. U., Warfield, S. K.: Highly accurate segmentation of brain tissue and subcortical gray matter from newborn MRI, *MICCAI*, 2006, 199–206.

[23] Wu, X.-L., Gai, J., Lam, F., Fu, M., Haldar, J. P., Zhuo, Y., Liang, Z.-P., Hwu, W.-M., Sutton, B. P.: Impatient MRI: Illinois Massively Parallel Acceleration Toolkit for image reconstruction with enhanced throughput in MRI, *Proceedings of ISBI International Society of Biomedical Imaging*, 2011, 69–72.